MoS$_2$ Nanosheets Uniformly Anchored on NiMoO$_4$ Nanorods, a Highly Active Hierarchical Nanostructure Catalyst for Oxygen Evolution Reaction and Pseudo-Capacitors

Getachew Solomon, Mojtaba Gilzad Kohan, Raffaello Mazzaro, Matteo Jugovac, Paolo Moras, Vittorio Morandi, Isabella Concina, and Alberto Vomiero*

Hierarchical nanostructures have attracted considerable research attention due to their applications in the catalysis field. Herein, we design a versatile hierarchical nanostructure composed of NiMoO$_4$ nanorods surrounded by active MoS$_2$ nanosheets on an interconnected nickel foam substrate. The as-prepared nanostructure exhibits excellent oxygen evolution reaction performance, producing a current density of 10 mA cm^{-2} at an overpotential of 90 mV, in comparison with 220 mV necessary to reach a similar current density for NiMoO$_4$. This behavior originates from the structural/morphological properties of the MoS$_2$ nanosheets, which present numerous surface-active sites and allow good contact with the electrolyte. Besides, the structures can effectively store charges, due to their unique branched network providing accessible active surface area, which facilitates intermediates adsorptions. Particularly, NiMoO$_4$/MoS$_2$ shows a charge capacity of 358 mAhg^{-1} at a current of 0.5 A g^{-1} (230 mAhg^{-1} for NiMoO$_4$), thus suggesting promising applications for charge-storing devices.

1. Introduction

Numerous alternatives have been explored and developed for advancing the technologies of the renewable energy sector. For overall water splitting, an efficient electrocatalyst capable of splitting water into its components is needed.[1–5] Low cost, high activity, and long-term stability in the electrolyte are the major criteria for an optimal electrocatalyst. To meet the

industrial standard of electrolysis, such criteria are critical and still challenging. For energy storage devices, such as super-capacitors, an active catalyst capable of providing high power density and superior cycle life is a necessary condition. Pseudo capacitors exhibit very high-power density similar to that of double-layer capacitor devices. However, they differ from a double-layer capacitor because of their battery-like redox processes of the charge storage principles. Transition metal oxides (TMOs) such as NiCo$_2$O$_4$@NiMoO$_4$,[6] NiCo-S (Fe-NiCo-S),[7] CoMxP/CC (M = Fe, Mn, and Ni),[8] and NiCoFe-P[9] have been employed as active electrocatalysts for OER and supercapacitors. Pseudocapacitive-type nanomaterials, especially TMOs or hydroxides, such as nickel oxide (NiO),[10,11] NiMoO$_4$@Co (OH)$_2$,[12] are widely investigated as candidates for supercapacitor applications due to their various oxidation states that contribute to the pseudo capacitance properties.

Hierarchical-structured catalysts have attracted considerable attention in the field of materials for renewable energy applications. These structures can effectively increase the active surface area owing to their morphology. We recently reported the catalytic efficiency of hydrated core NiMoO$_4$ and shell Co$_3$O$_4$

G. Solomon, M. G. Kohan, I. Concina, A. Vomiero
Division of Materials Science
Department of Engineering Sciences and Mathematics
Luleå University of Technology
Luleå SE-971 87, Sweden
E-mail: alberto.vomiero@ltu.se
R. Mazzaro, V. Morandi
Istituto di Microelettronica e Microsistemi-CNR (CNR, IMM)
Via Piero Gobetti 101, Bologna 40129, Italy

R. Mazzaro
Department of Physics and Astronomy
University of Bologna
Via Berti Pichat 6/2, Bologna 40129, Italy
M. Jugovac
Elettra Sincrotrone Trieste
SS 14 Km 163,5, Trieste 34149, Italy
M. Jugovac, P. Moras
Istituto di Struttura della Materia-CNR (ISM-CNR)
SS 14, Km 163,5, Trieste 34149, Italy
A. Vomiero
Department of Molecular Sciences and Nanosystems
Ca' Foscari University of Venice
Via Torino 155, Venezia Mestre, Bologna 30172, Italy

**ADVANCED
SCIENCE NEWS**

www.advancedsciencenews.com

**ADVANCED
SUSTAINABLE
SYSTEMS**

www.advsustainsys.com

heterostructure towards OER, for which we revealed that the high catalytic activity is due to the in situ catalysts reconstruction process and leaching out of Mo atom from crystalline $NiMoO_4$ structure.[13] Motivated by that result, we extended the work by wrapping the hydrated $NiMoO_4$ nanorods with two-dimensional MoS_2 nanosheets. It is known that the presence of MoS_2 together with other nanostructures can enhance the properties of different composites, Bu modulating the exposed surface area of the nanostructure.[14,15] It was reported that interconnected hierarchical nanosheets exhibit an improved surface area that enhances the adsorption or intercalation of reaction intermediates, due to the ease of electrolyte diffusion throughout the structure.[16] MoS_2 nanosheets present a promising catalyst for the hydrogen evolution reaction (HER).[17] MoS_2 nanosheets are effectively used in altering the surface properties of charge-storing devices due to their outstanding capacitive performance.[16–19]

Hierarchical nanostructure (like the trees with trunks and branches) provides a perfect contact area with electrolytes. Thanks to the nondestructive synthesis methods of magnetron sputtering, the morphology of $NiMoO_4$ nanorods was preserved. We believe that this strategy, involving the construction of vertically aligned nanorods with subsequent MoS_2 wrapping on the nanorods, can efficiently improve the electrochemically active surface area, allowing it to be extended to many electrochemical applications. Besides, the use of hierarchical nanostructures can benefit from enhanced electrolyte penetration and avoiding particle agglomeration. $NiMoO_4$ possesses a very high specific capacitance and conductivity due to its excellent redox activity and the ability to accommodate several oxidation states. The decorated nanosheet layers can also store charges and induce a faradaic charge transfer process. As a result, the synergistic effect arising from $NiMoO_4$ and MoS_2 could enhance the electrochemical properties of the hierarchical structure ($NiMoO_4$/MoS_2). To the best of our knowledge, the OER activity of $NiMoO_4$/MoS_2 is not explored yet.

2. Results and Discussion

2.1. Structural and Morphological Characterizations

Scanning electron microscopy (SEM) images of the hierarchical $NiMoO_4$/MoS_2 nanostructure (**Figure 1**) show that the micro rods are vertically oriented and grown on a Nickel foam substrate. $NiMoO_4$ grown by optimizing the precursors and synthesis temperature produces well-aligned vertically grown smooth nanorods (Figure 1a). The deposition of MoS_2 via magnetron sputtering is performed for 30 min, with a rate of around $0.5 \, nm \, s^{-1}$, calculated by combining the deposition duration, cross-sectional SEM, and RBS analyses, which were also characterized in our recent work.[20] The morphology of MoS_2 deposited for 7 min (for comparison purposes, Figure S1a, I), displays a spot of nanoparticles, leaving most of the $NiMoO_4$ nanorods uncovered. However, for the 30 min MoS_2 deposition (Figure 1c,d), the as-synthesized $NiMoO_4$ rods are completely covered and interconnected nanosheets are visible.

The MoS2 nanoflakes are grown homogeneously all over the nanorods, decorating the NiMoO4 nanostructure. The construction of the hierarchical $NiMoO_4$/MoS_2 nanostructure can be
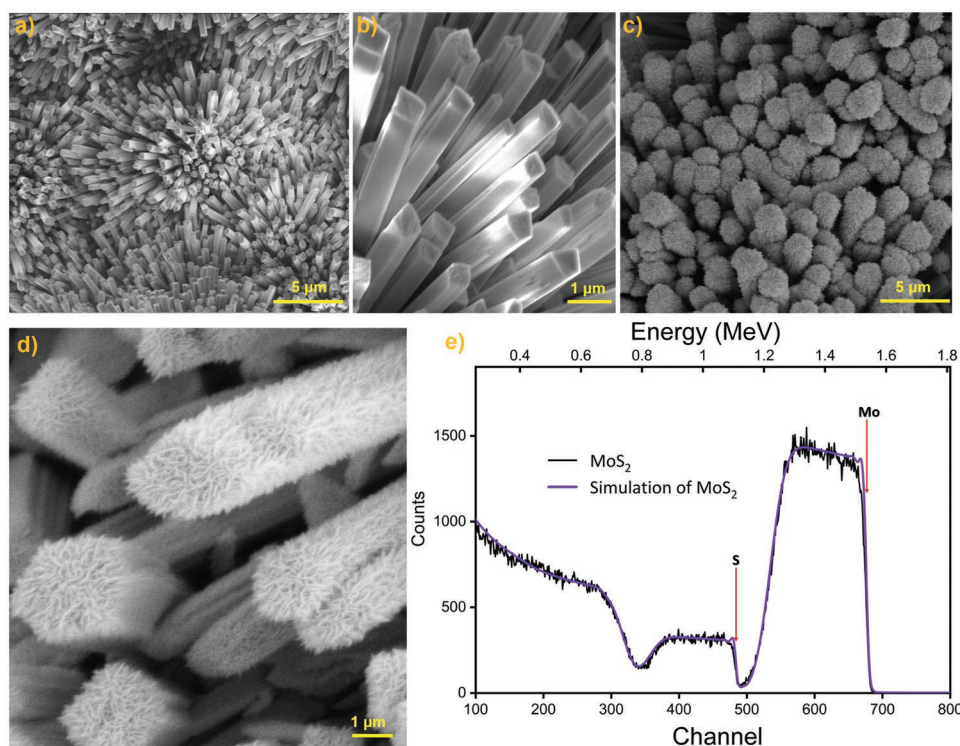
Figure 1. Morphological and structural characterization: SEM images for a,b) $NiMoO_4$, and c,d) MoS_2 wrapping $NiMoO_4$ micro-rods, e) RBS with corresponding x-RUMP code simulations spectra for MoS_2. The surface edges for Mo and S are indicated by the vertical arrows.
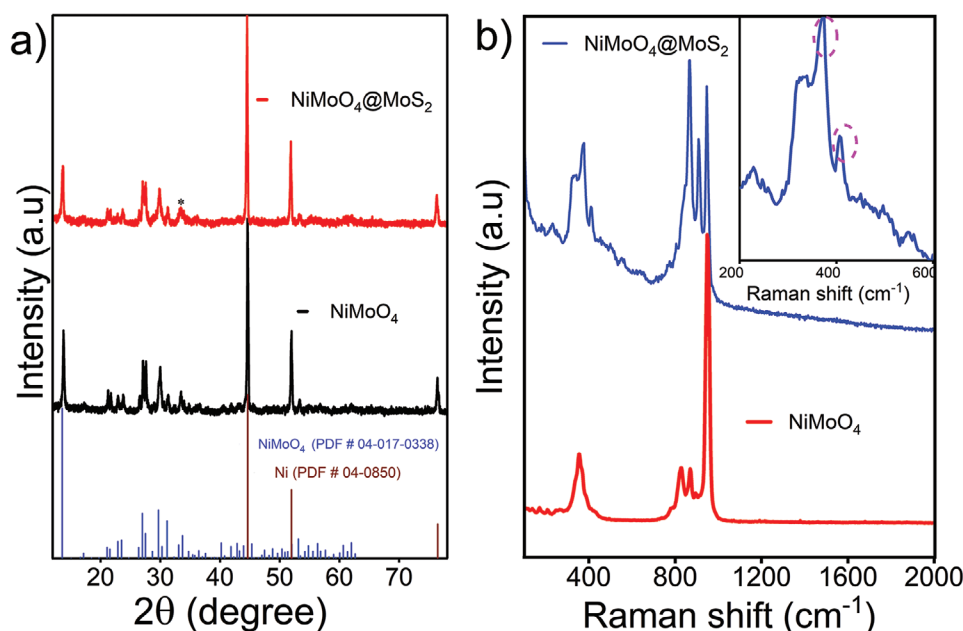
Figure 2. a) X-ray diffraction spectra of $NiMoO_4/MoS_2$ (red) and $NiMoO_4$ (black), Bottom line: expected reflections from $NiMoO_4$ (blue), nickel substrate (wine). b) Raman spectra of $NiMoO_4$ (red) and $NiMoO_4/MoS_2$ (blue), with an inset showing the resolution of the Raman peak for MoS_2 at 378 and 408 cm^{-1} associated with E_{12g} and A_{1g} vibration modes of MoS_2.

easily recognized in the SEM images. Hierarchical nanostructure created due to the strong attachment of MoS_2 nanosheets can be beneficial for improving the catalysis process because it can easily provide an extra pathway for ions and electrons transport at the interface. (Figure 1e) shows the RBS spectra of MoS_2 with a uniform in-depth distribution of all the detected elements. The increased yield of the high-energy signal marked by the arrows confirms the presence of Mo and S. The atomic ratio for Mo:S is calculated as 1:1.5 with the help of RUMP code simulations (in agreement with our previous work[20]).
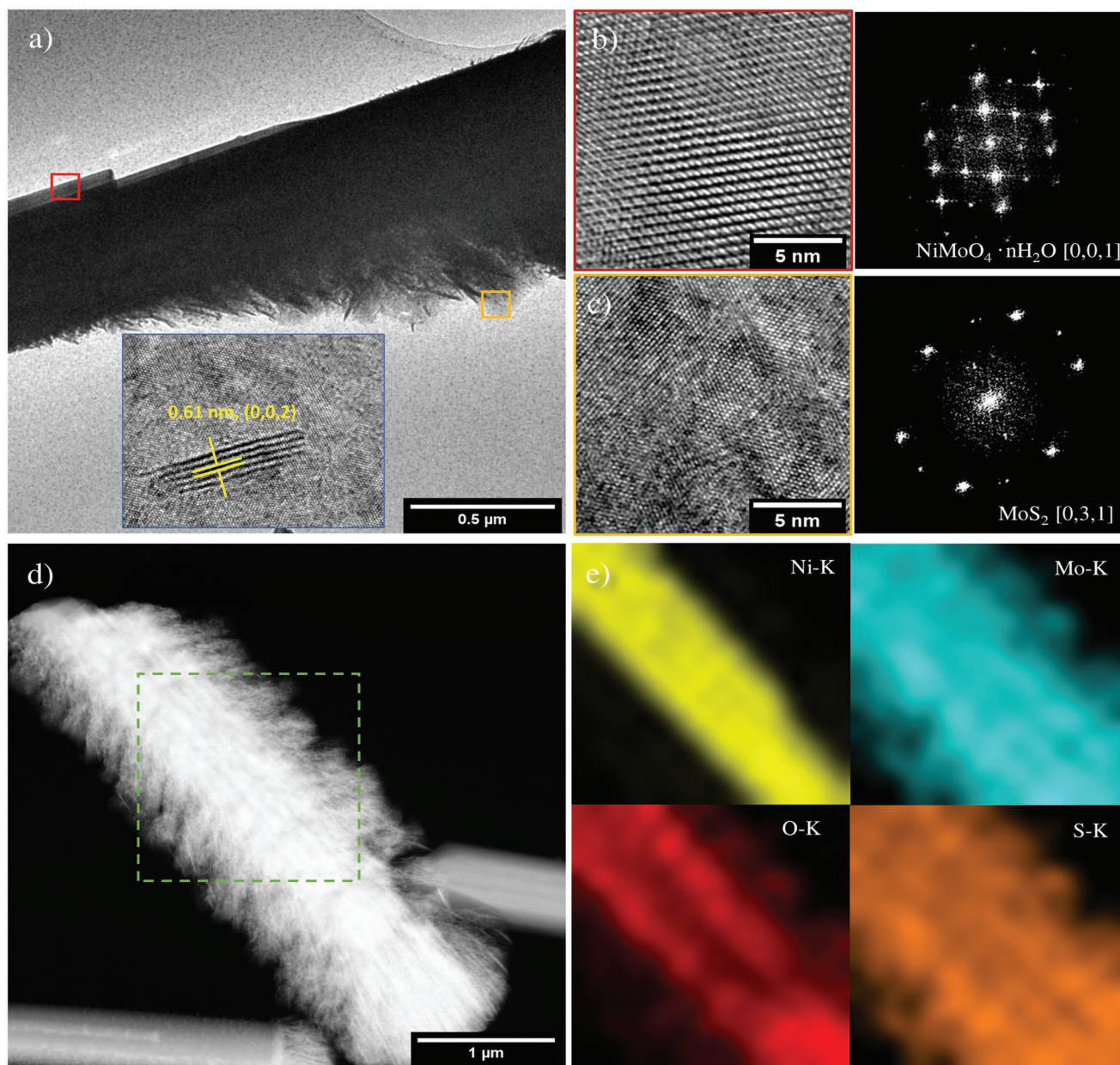
The composition and phase structure of as-synthesized nanostructure were investigated by XRD and Raman spectra. XRD patterns of $NiMoO_4$ and $NiMoO_4/MoS_2$ (**Figure 2**a) confirm the presence of hydrated $NiMoO_4$. The intense peaks at $2\theta = 44.4°$, 51.8°, and 76.3° correspond to the nickel substrate, indexed by PDF# 04–0850. The remaining peak corresponds to the diffraction pattern of hydrated nickel molybdate ($NiMoO_4.xH_2O$), referenced by PDF# 04-017-0338.[21] For simplicity, we named the $NiMoO_4.xH_2O$ as $NiMoO_4$. The XRD pattern of $NiMoO_4$ is not affected by the addition of MoS_2. The reflection at $2\theta = 33.4°$ (labeled asterisks), which is broad compared to the XRD peak of $NiMoO_4$, confirms the presence of MoS_2.[17,22]

The weak XRD pattern of MoS_2 is overlapped with the strong peak of $NiMoO_4$, and some of the reflections pertaining to MoS_2 are not completely visible in the diffraction pattern. We observed a similarly broad and weak XRD peak for sputtered MoS_2.[17,23] The Raman spectrum of $NiMoO_4$ (Figure 2b) displays an intense peak at 949 cm^{-1} (due to a symmetric Mo=O bond), at 869 cm^{-1} and at 826 cm^{-1} (due to an asymmetric Mo=O bond), and a broad peak at 356 cm^{-1} (due to Mo–O bending).[21,24,25] The intensity of the Raman band associated with $NiMoO_4$ decreased due to the presence of MoS_2. The two characteristic bands at ≈378 and ≈408 cm^{-1} associated

with E_{12g} and A_{1g} vibration modes of MoS_2, respectively (see inset of Figure 2b), clearly show the presence of 2H MoS_2 nanosheets.[23]

MoS_2 sputtering deposition results in an anisotropic coating of pristine $NiMoO_4$, as highlighted by HR-TEM and low-magnification micrographs (**Figure 3**a). The nanowire coating degree depends on the relative nanowire orientation during the sputtering process and the portion of nanowire considered for the analysis, ranging from almost pristine $NiMoO_4$ nanowires to fully covered ones (Figure S1, Supporting Information). The hydrated $NiMoO_4$ nanowires crystal phase is confirmed by high magnification micrographs, as well as MoS_2 one (Figure 3b,c), whose crystallinity degree varies in different areas of the sample. The high-magnification micrographs display a lattice spacing of 0.63 nm, corresponding to the (002) plane of the hexagonal MoS_2, which is consistent with the interlayer spacing of hexagonal 2H-MoS_2.[20] STEM-EDS mapping of a fully coated NW displays the selective concentration of Ni-Kα signal in the core of the nanowire, while Mo and S have homogeneously distributed over all the heterostructure, confirming the distribution of all elements across the hierarchical structures (Figure 3d,e and Figures S2 and S3, Supporting Information). The O-related signal is also located in the core of the heterostructure, but it is worth noticing a slight background signal on the shell area, suggesting the possible presence of surface oxide impurities, resulting from partial oxidation of the sulfide structures during the sputtering process.

XPS was used to characterize the elemental compositions and chemical valence of the $NiMoO_4/MoS_2$, and $NiMoO_4$ systems (**Figure 4**). The most intense core level lines in the overview spectrum of $NiMoO_4/MoS_2$ (Figure 4a) are attributed to C1s, Mo3d, and S2p and weaker features to O1s, S2s, Mo4s, and Mo4p. No Ni signal is detected due to the thickness of the MoS_2
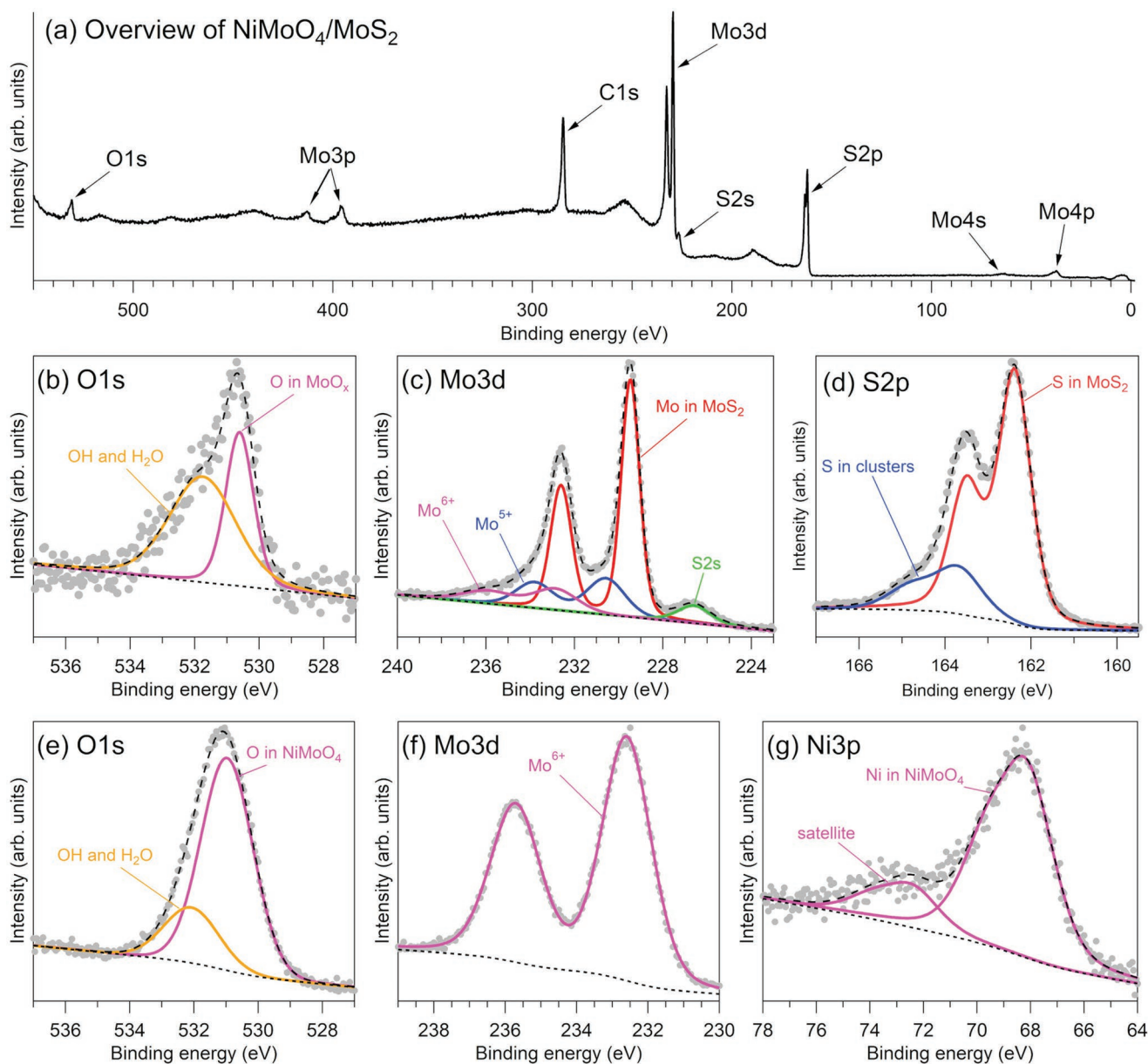
**ADVANCED
SCIENCE NEWS**

www.advancedsciencenews.com

**ADVANCED
SUSTAINABLE
SYSTEMS**

www.advsustainsys.com

Figure 3. a) Low magnification and HR-TEM micrograph for the MoS_2 decorated $NiMoO_4$ sample displaying the anisotropic deposition of MoS_2. In the inset, high magnification detail of the MoS_2 coated side exhibits reflections compatible with (0, 0, 2) lattice planes. b,c) High-resolution micrograph of selected areas (edge color corresponding to the highlighted area) of the same nanowire displayed in (a) and corresponding FFT, representing the typical lattice observed on the nanowire core and the decorating nanoflakes, respectively. d) STEM-HAADF micrograph of MoS_2 decorated $NiMoO_4$ nanowire with e) relative distribution of EDS Kα peaks for Ni, Mo, O, and S, confirming the core-shell structure.

layer covering the $NiMoO_4$ micro-rods and the Ni foam substrate. The O1s spectrum (Figure 4b) presents two components at 530.6 eV, ascribed to the presence of MoO_x, and at 531.8 eV, due to the presence of OH groups and adsorbed water. The Mo3d spectrum can be fitted with three doublets (the rightmost peak in Figure 4c is attributed to S2s emission).

The energy position of the Mo3d$_{5/2}$ peaks of the doublets is 229.5, 230.6, and 232.8 eV and corresponds to Mo^{4+} (in 2H-MoS_2), Mo^{5+}, and Mo^{6+}, respectively. The last component confirms the presence of Mo oxides on the surface of the

system (unreacted metallic Mo that oxidizes in contact with air). The other two components find their counterpart in the S2p spectrum (Figure 4d), which is well described by two doublets. The dominant component (S2p$_{3/2}$ at 162.4 eV) derives from S^{2-} in 2H-MoS_2. The other component (S2p$_{3/2}$ at 163.7 eV) is connected to the presence of Mo$_3$–S and Mo–S$_3$ clusters, in which Mo shows the Mo^{5+} oxidation state.[26] As a reference, we report in the bottommost row of Figure 4 the O1s, Mo 3d, and Ni3p core levels of the hydrous $NiMoO_4$ micro-rods. The two components describe the O1s spectrum in Figure 4e: the

**ADVANCED
SCIENCE NEWS**

www.advancedsciencenews.com

**ADVANCED
SUSTAINABLE
SYSTEMS**

www.advsustainsys.com

Figure 4. High-resolution XPS spectra of the $NiMoO_4/MoS_2$ (top and central rows) and $NiMoO_4$ (bottom row) systems. a) Overview scan, b) O1s, c) Mo3d, and d) S2p spectra. e) O1s, f) Mo3d, and g) Ni 3p spectra.

main peak at 531.0 eV is attributed to O in $NiMoO_4$, and the peak at 532.1 eV to OH groups and water. The Mo3d spectrum of Figure 4f is fitted with one doublet associated with Mo^{6+} ($Mo3d_{5/2}$ at 232.6 eV) in $NiMoO_4$.[27–29] The Ni3p spectrum of Figure 4g, shows only one doublet ($Ni3p_{3/2}$ at 68.1 eV) and the related satellite feature ($Ni3p_{3/2}$ at 72.3 eV). This Ni^{2+} is correlated to the presence of $NiMoO_4$.[13,30]

2.2. Electrochemical Characterizations

The OER catalytic performances of the hierarchical structures ($NiMoO_4/MoS_2$) and bare $NiMoO_4$ are investigated using linear sweep voltammetry (LSV) by a three-electrode system.

Both $NiMoO_4$ and $NiMoO_4/MoS_2$ catalysts prove their catalytic activity, evidenced by the increase in current density after the onset potential (**Figure 5**a). Thanks to the presence of highly active MoS_2, the heterostructure ($NiMoO_4/MoS_2$) displays a dramatic shift of the onset potential to less positive values (lower overpotential). In particular, $NiMoO_4/MoS_2$ results in a current density of 10 mA cm^{-2} at an overpotential of 90 mV, while $NiMoO_4$ needs 223 mV to reach a similar current density. The lowest overpotential (90 mV), evidenced by the fastest increase in the current density of $NiMoO_4/MoS_2$, demonstrates the importance of MoS_2 in modifying the catalyst surface/interface properties for better electrochemical activity.

The Tafel plot, derived from the polarization curve (Figure 5b), provides additional information on the kinetics of
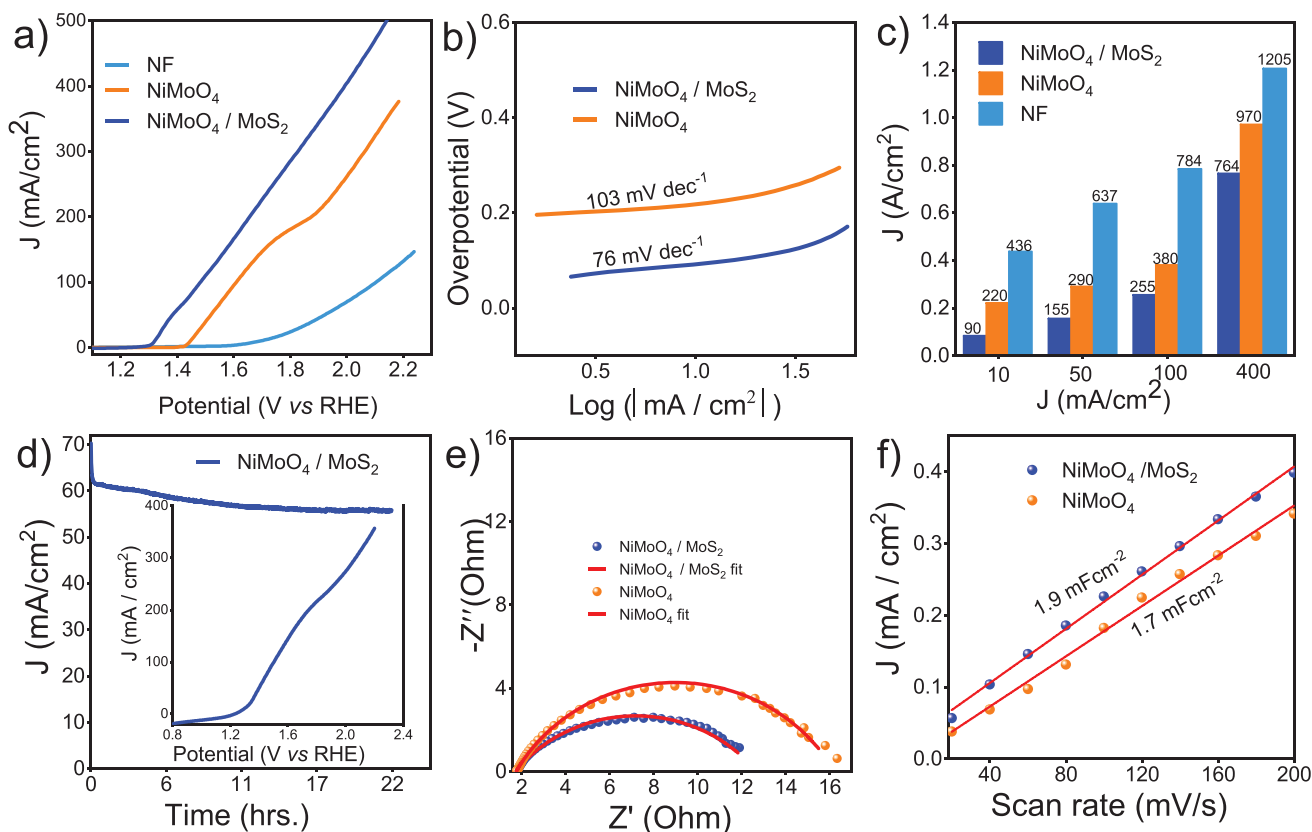
Figure 5. OER performance of the catalyst. a) Polarization curves of NiMoO$_4$/MoS$_2$, NiMoO$_4$, and nickel foam. b) Corresponding Tafel plots of the catalysts (NiMoO$_4$/MoS$_2$, NiMoO$_4$). c) Overpotential at different current densities, d) stability (chronoamperometry measurement) for NiMoO$_4$/MoS$_2$ (the inset shows the LSV after the stability test), and e,f) Nyquist plot at 1.45 V, C_{dl} extracted from cyclic voltammetry for NiMoO$_4$/MoS$_2$ and NiMoO$_4$.

the OER process on the catalyst surfaces. NiMoO$_4$/MoS$_2$ possesses a Tafel slope of 76 mV dec^{-1}, which is lower compared to NiMoO$_4$ (103 mV dec^{-1}), suggesting a faster kinetics during the OER process of the NiMoO$_4$/MoS$_2$ catalyst. The overpotential at different current densities was also computed for both catalysts and displayed in Figure 5b. In addition to the overpotential value producing 10 mA cm^{-2}, NiMoO$_4$/MoS$_2$ current density of 50, 100, and 200 mA cm^{-2} at overpotentials equal to 155, 255, and 430 mV, respectively. Similarly, the same current densities are produced by NiMoO$_4$ with 311, 409, and 730 mV overpotentials. Compared to our previous work,[13] the bare NiMoO$_4$ in the present study shows a minor decrease in the overall performance due to the heat treatment in the PVD chambers. Moreover, an OER rate of 10 mA cm^{-2} for the NiMoO$_4$/MoS$_2$ can be readily attained by applying a small-scale overpotential (90 mV), which is very low compared to recently published works.[31–35] For comparison purposes, the substrate NF was also characterized in terms of LSV and overpotential (Figure 5a,c). we have also compared the electrochemical properties of the MoS$_2$ catalyst using our recently published work, for which MoS$_2$ requires an overpotential of 500 mV to produce a current density of 100 mA cm^{-2}.[20] However, NiMoO$_4$/MoS$_2$ structure needs 250 mV to produce a similar current density, demonstrating the electrocatalytic phenomena behind the hierarchical structure of composites for improving OER catalyst.

Long-term stability tests were performed using chronoamperometry at a potential of 1.40 V versus RHE by producing a constant current density of 60 mA cm^{-2}. The hierarchical heterostructure shows a decrease in current density for the first few hrs (Figure 5d, inset), suggesting the detachment of loosely attached MoS$_2$ nanosheets from the NiMoO$_4$ nanorods. However, it is clear that the performance of hierarchical heterostructure improved after the incorporation of MoS$_2$ nanosheets. Besides, NiMoO$_4$ maintains its long-term stability at 1.53 V versus RHE to produce a current density of 50 mA cm^{-2} for nearly 18 h, with negligible losses, as shown in Figure S3, Supporting Information. EIS is used to elucidate the charge transfer kinetics, as displayed in Figure 5e. The EIS spectra are collected at a DC potential of 1.45 V versus RHE, for which the charge transfer process is kinetically controlled. An associated fitting for the EIS data is displayed in Table S1, Supporting Information. Since the catalyst surface is rough and porous, the impedance analysis contains constant phase elements (CPE) rather than pure capacitors. The decrease in the charge-transfer resistance for NiMoO$_4$/MoS$_2$ (10.9 Ω) compared to pure NiMoO$_4$ (14.4 Ω) indicates that the hierarchical heterostructure has a much faster electron transfer during the electrochemical reaction, arising from the existence of NiMoO$_4$ and MoS$_2$ phases. It is also consistent with its lower Tafel slope, which corresponds with the improved electrocatalytic performance.

The electrochemical active surface area (ECSA) is evaluated by measuring the double-layer capacitance (C_{dl}) using CV recorded from 1.1–1.20 V (vs RHE) (Figure S5, Supporting Information). The double-layer capacitance derived from the CV provides an estimation of the ECSA of NiMoO$_4$/MoS$_2$ (1.9 mF cm^{-2}) and NiMoO$_4$ (1.7 mF cm^{-2}). These minor differences in C_{dl} suggest only a minor increase of ECSA for the heterostructure, suggesting that both catalysts provide nearly similar accessible and abundant reaction sites in non-faradic regions. The enhanced catalytic activity observed in the case of the hierarchical structure can, therefore, be attributed to the altered intrinsic activity rather than the geometrical factor. The electrochemical performance indicates that the hierarchical NiMoO$_4$/MoS$_2$ is an electrocatalyst material with superior OER activity and stability under alkaline conditions. It can be seen that after a long stability test, the morphology of the heterostructure preserves as observed in Figure S6, Supporting Information. The inherently high activity of the NiMoO$_4$ is believed to be responsible for the improvement of electrocatalytic performance. For instance, in our recent work [13] we have shown that during the OER process, hydrous NiMoO$_4$ undergoes an in situ transformation into NiOOH, with the dissolution of Mo species. Especially, the leaching of Mo species creates voids that are active toward the OER, allowing to improve the electrochemical activity. In this work, the presence of thick MoS$_2$ protects the hydrated NiMoO$_4$ and makes it difficult to detect the dissolution of Mo from NiMoO$_4$ nanorods. In many works, catalysts containing Ni, Fe-doped nickel oxides, and hydroxides of Ni were very active as water oxidation catalysts in alkali electrolytes.[34,36] This is because the Ni redox process on the surface occurring at lower anodic potential activities alters the catalyst surface to become more active and rougher during the reaction. Therefore, it is reasonable to state that the presence of hydrated NiMoO$_4$ is also responsible for the outstanding performance of the catalyst. Also, the hierarchical nanostructure results in increased porosity of the electrode, which improves the contact area of the interface, facilitating electrolyte diffusion through the entire hierarchical nanostructure.

Very interestingly, the hierarchical NiMoO$_4$/MoS$_2$ nanostructure can be also used as a charge storage device. Thanks to the very active site densities created at the surface/interface of NiMoO$_4$ due to the presence of MoS$_2$ nanosheets, the heterostructure becomes an excellent candidate for supercapacitors. We measured the capacitance of the as-obtained NiMoO$_4$@MoS$_2$ composite using cyclic voltammetry and galvanostatic charge-discharge (GCD) in a three-electrode system, as shown in **Figure 6**a–d. The charge storage mechanisms in pseudocapacitive materials possess battery-like charge-discharge properties. Therefore, the specific charge capacity (Cs) of the prepared samples is calculated from the GCD curves using Equation (1).[37–39]

$$C_s\left(Ahg^{-1}\right) = \frac{\int i(A)\,dt(s)}{3600 \times m(g)} \tag{1}$$

where i, t, and m are the applied current density (A), discharge time (s), and the active mass of material (g), respectively. The mass of the active sample was obtained by subtracting the substrate NF. Here the active mass is 1 mg cm^{-2}.
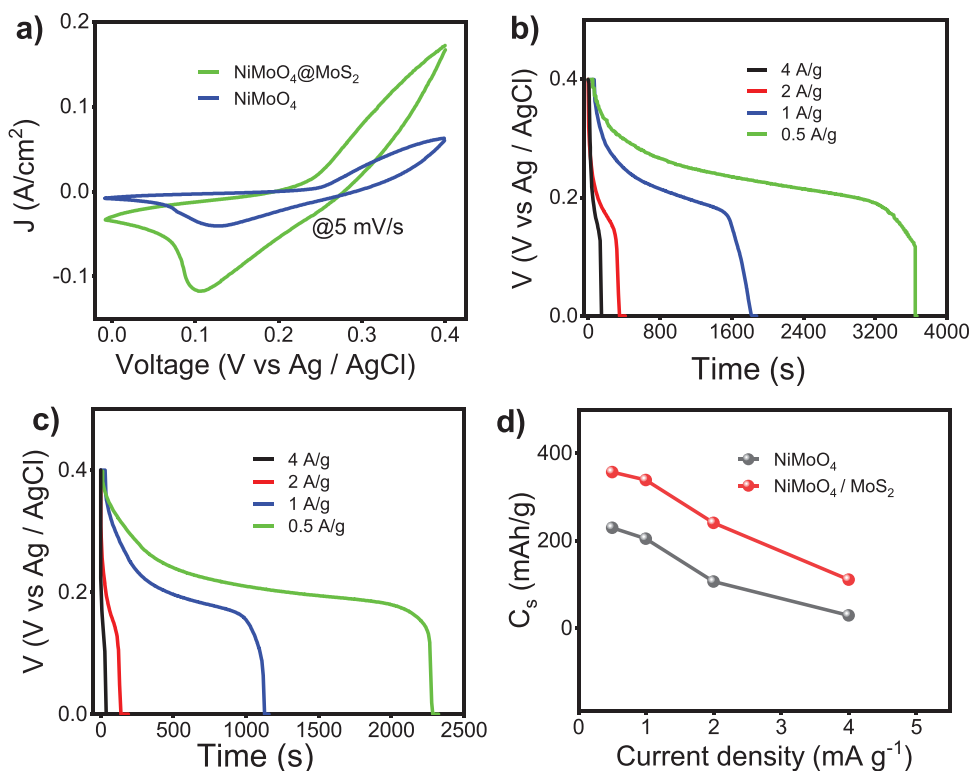
Figure 6. a) Cyclic voltammetry curves for hierarchical NiMoO$_4$/MoS$_2$ and NiMoO$_4$ at a scan rate of 5 mVs^{-1}. b,c) Galvanostatic discharge curves for NiMoO$_4$/MoS$_2$ and NiMoO$_4$ respectively. d) Specific charge capacities of NiMoO$_4$/MoS$_2$ and NiMoO$_4$ at various current density.

**ADVANCED
SCIENCE NEWS**

www.advancedsciencenews.com

**ADVANCED
SUSTAINABLE
SYSTEMS**

www.advsustainsys.com

The CV curve for $NiMoO_4/MoS_2$ and $NiMoO_4$ (Figure 6a) displays a redox peak in the reverse scan (repeated CV measurement performed to produce a stable CV curve). By comparing the CV curves, we reveal that the capacity for $NiMoO_4/MoS_2$ is larger than that of pristine $NiMoO_4$, evidenced by the larger integrated area of the corresponding curve. The discharge capacity of the hierarchical $NiMoO_4/MoS_2$ and $NiMoO_4$ was measured at different currents (Figure 6b,c).

The specific charge capacity is calculated from each discharge curve using Equation (1) and displayed in Figure 6c. At discharge currents of 0.5, 1, 2, and 4 A g^{-1}, the $NiMoO_4/MoS_2$ and $NiMoO_4$ nanostructure can reach 358, 339, 241, 111 and 230, 205, 107, 28 mAh g^{-1}, respectively. Clearly, the hierarchical nanostructure exhibits an improvement in specific charge capacity due to the presence of MoS_2 nanosheets. The hierarchical $NiMoO_4/MoS_2$ nanostructure results in up to 1.8 times longer discharge rate compared to $NiMoO_4$, at 0.5 A g^{-1}. Besides, we evaluated the stability/reversibility of the nanostructures (Figure S7, Supporting Information), exhibiting good cycling durability, with 94% for $NiMoO_4/MoS_2$ and 85% for $NiMoO_4$ after 2000 charge-discharge cycles. . The last 10 charge-discharge cycles of the 2000 cycle are also presented in Figure S7c, Supporting Information. Furthermore, the energy storage mechanism for NiMoO4/MoS2 and NiMoO4 was analyzed with help of the relationship between peak potential and cathodic sweep rate.[9,40,41] As shown in Figure S7e, Supporting Information. The calculated b value of the cathodic NiMoO4/MoS2 is 0.51, suggesting the charge storage principle is a battery-like characteristic.[9,40,41] The higher performance of $NiMoO_4/MoS_2$ nanostructure is justified mainly due to the high conductivity of $NiMoO_4$, and the porous and interconnected MoS_2 nanosheets surrounding the nanorods which provide a path for ion transport between the interface and electrolyte. In addition, $NiMoO_4$ can create NiOOH in situ, which can offer further surface redox sites due to the conversion between nickel (II) and nickel (III) species. This redox activity at the surface accounts for the enhancement of the charge storage of hierarchical nanostructure, contributing to the higher specific charge capacity. Furthermore, the presence of MoS_2 nanoflakes is beneficial; because it promotes the electrochemical properties of active materials by providing an extra active site density, assisting the adsorption of oxygen intermediates, and accelerating the bubble release rate by providing additional surface areas.

3. Conclusion

We described a method to develop efficient hierarchical electrocatalysts for OER and charge storage applications through an easy and scalable method. A hierarchical structure is fabricated by modifying the $NiMoO_4$ nanosheets with MoS_2 nanosheets: MoS_2 nanosheets uniformly surrounding the nanorods improve the electrochemical properties of the hierarchical nanostructure. The interconnected porous network also helps to effectively store ions and charges that improve OER activity and the charge-storing capacity. Moreover, the $NiMoO_4/MoS_2$ displays a very low overpotential (90 mV) to produce a current density of 10 mA cm^{-2}, which is one of the minimum overpotentials among the ones reported in the literature. Furthermore, at a discharge current of 0.5 A g^{-1}, the hierarchical nanostructure displays 358 mAh g^{-1} charge storage capacity, up to 1.8 times a longer discharge rate than $NiMoO_4$. This work shows the benefit of hierarchical nanostructure in altering the charge transfer process and improving the performance of the catalyst.

4. Experimental Section

NiMoO₄ Synthesis: Hierarchical $NiMoO_4/MoS_2$ nanostructure was fabricated by first hydrothermally synthesizing $NiMoO_4$ followed by a subsequent magnetron sputtering process. First, commercial nickel foam (NF) was cleaned using an ultrasonic bath in 3 M HCl (to remove oxide) for 15 min followed by a 15 min wash with acetone, ethanol, and distilled water. Then, a piece of NF (4 × 6 cm^2) was placed inside a 100 ml hydrothermal reaction vessel containing 1 g $Ni(NO_3)_2 \cdot 6H_2O$, 0.5 g $(NH_4)6Mo_7O_{24} \cdot 4H_2O$, and 75 ml of distilled water. Finally, the vessel was sealed and maintained at 140 °C for 6 h. The reaction product was washed with ethanol and distilled water and dried overnight at 60 °C. The obtained structure was a hydrated $NiMoO_4$, labeled as $NiMoO_4$. MoS_2 deposition was performed by magnetron sputtering as described in our previous work.[20] The molybdenum sulfide target, MoS_2, 99.95% pure, 3.00″ diameter, was used as a source for magnetron sputtering. The deposition was performed for 30 min, with a rate of around 0.5 nm s^{-1}, calculated by combining the deposition duration, cross-sectional SEM, and RBS analyses. During the deposition, the substrates were heated at 200 °C in an argon atmosphere. To avoid the difference that may arise due to the heating process in the PVD chamber during MoS_2 deposition, the bare $NiMoO_4$ nanorods were subjected to heating in a similar condition used for MoS_2 deposition.

Characterization: The morphology and composition of $NiMoO_4/MoS_2$ nanorods were characterized by Magellan 400 field emission scanning electron microscopy (FESEM), and transmission electron microscopy (TEM). Elemental analysis was conducted using energy-dispersive X-ray spectroscopy (EDX) in the FESEM. X-ray diffraction patterns (XRD) were recorded on the PANalytical Empyrean X-ray diffraction diffractometer with a Cu Kα source. Raman analysis was carried out using a Senterra Raman spectrometer from Bruker equipped with a 532 nm laser for excitation) in the ambient environment. Rutherford backscattering spectrometry (RBS) was carried out for analyzing the composition and thickness of the film. 1.8 MeV $^4He^+$ beam in IBM geometry was used. The scattering angle was $\theta = 160°$. Sampled was deposited on Silicon. The analysis was performed on samples deposited on silicon under a similar condition to MoS_2. The RBS spectrum was analyzed with the help of RUMP code simulation.

X-ray Photoelectron Spectroscopy (XPS) analysis was carried out at the VUV-Photoemission beamline of the synchrotron Elettra in Trieste (Italy). XPS spectra were collected using a Scienta R-4000 electron spectrometer with 700 and 690 eV photon energy for the $NiMoO_4/MoS_2$ and $NiMoO_4$ systems, respectively, and 250 meV total energy resolution. The data were analyzed using Voigt line shape peaks. The base pressure during the XPS experiments was below 5 × 10^{-10} mbar. The binding energy (BE) scale was calibrated by using adventitious carbon at 284.6 eV.

High-resolution transmission electron microscopy (HR-TEM) characterization was performed on FEI Tecnai F20 TEM, equipped with a Schottky emitter operating at 200 kV, Energy dispersive X-ray spectrometer (EDS), and high angle annular dark field for scanning TEM imaging (STEM-HAADF).

Electrochemical Measurements: The electrocatalytic performance test and electrochemical impedance spectroscopic (EIS) analysis of the as-synthesized catalysts was performed using a three-electrode system at room temperature in a multi-purpose electrochemical workstation potentiostat (Solartron Analytical, ModulabXM). Saturated calomel electrode (SCE) and platinum foil were used as the reference and

**ADVANCED
SCIENCE NEWS**

www.advancedsciencenews.com

**ADVANCED
SUSTAINABLE
SYSTEMS**

www.advsustainsys.com

counter electrodes, respectively. Linear sweep voltammetry (LSV) was conducted in 1 M KOH, with a scan rate of 10 mV s^{-1}. The potential of the reference electrode was converted to a reversible hydrogen electrode (RHE) by the relation: E(RHE) = E(SCE) + 0.059*pH + 0.242 with pH = 14. EIS was measured over the frequency spectrum range from 100 kHz to 50 MHz at an Ac amplitude of 10 mV. The polarization curves were manually IR compensated. Chronoamperometry measurement was performed for stability tests.

Supporting Information

Supporting Information is available from the Wiley Online Library or from the author.

Conflict of Interest

The authors declare no conflict of interest.

Data Availability Statement

The data that support the findings of this study are available in the supplementary material of this article.

[1] X. Li, L. Zhao, J. Yu, X. Liu, X. Zhang, H. Liu, W. Zhou, *Nano-Micro Lett.* **2020**, *12*, 131.

[2] Z. Chen, X. Duan, W. Wei, S. Wang, B. J. Ni, *J. Mater. Chem. A* **2019**, *7*, 14971.

[3] X. Peng, C. Pi, X. Zhang, S. Li, K. Huo, P. K. Chu, *Sustainable Energy Fuels* **2019**, *3*, 366.

[4] V. S. Bagotskii, L. N. Nekrasov, N. A. Shumilova, *Russ. Chem. Rev.* **1965**, *34*, 717.

[5] X. Ge, A. Sumboja, D. Wuu, T. An, B. Li, F. W. T. Goh, T. S. A. Hor, Y. Zong, Z. Liu, *ACS Catal.* **2015**, *5*, 4643.

[6] D. Cheng, Y. Yang, J. Xie, C. Fang, G. Zhang, J. Xiong, *J. Mater. Chem. A* **2015**, *3*, 14348.

[7] R. Liu, S. Xu, X. Shao, Y. Wen, X. Shi, L. Huang, M. Hong, J. Hu, Z. Yang, *ACS Appl. Mater. Interfaces* **2021**, *13*.

[8] X. Zhang, C. Sun, S. Xu, M. Huang, Y. Wen, X. R. Shi, *Nano Res.* **2022**, *15*, 8897.

[9] R. Liu, X. R. Shi, Y. Wen, X. Shao, C. Su, J. Hu, S. Xu, *J Energy Chem* **2022**, *74*, 149.

[10] S. Yang, X. Wu, C. Chen, H. Dong, W. Hu, X. Wang, *Chem. Commun.* **2012**, *48*, 2773.

[11] P. G. Schiavi, P. Altimari, F. Marzolo, A. Rubino, R. Zanoni, F. Pagnanelli, *J. Alloys Compd.* **2021**, *856*, 157718.

[12] W. Ren, D. Guo, M. Zhuo, B. Guan, D. Zhang, Q. Li, *RSC Adv.* **2015**, *5*, 21881.

[13] G. Solomon, A. Landström, R. Mazzaro, M. Jugovac, P. Moras, E. Cattaruzza, V. Morandi, I. Concina, A. Vomiero, *Adv. Energy Mater.* **2021**, *11*, 2101324.

[14] L. Yang, Z. Jin, J. Zheng, B. Zhang, J. Xu, X. B. Yin, M. Zhang, *Inorg. Chem.* **2022**, *61*, 542.

[15] H. Peng, J. Zheng, B. Zhang, J. Xu, M. Zhang, *Dalton Trans.* **2021**, *50*, 15380.

[16] N. Joseph, P. M. Shafi, A. C. Bose, *Energy Fuels* **2020**, *34*, 6558.

[17] G. Solomon, R. Mazzaro, V. Morandi, I. Concina, A. Vomiero, *Crystals* **2020**, *10*, 1040.

[18] Q. Ke, X. Zhang, W. Zang, A. M. Elshahawy, Y. Hu, Q. He, S. J. Pennycook, Y. Cai, J. Wang, Q. Ke, W. Zang, A. M. Elshahawy, Y. Hu, S. J. Pennycook, J. Wang, X. Zhang, Q. He, Y. Cai, *Small* **2019**, *15*, 1900131.

[19] S. Guan, X. Fu, Z. Lao, C. Jin, Z. Peng, *ACS Sustain Chem Eng* **2019**, *7*, 11672.

[20] G. Solomon, M. G. Kohan, M. Vagin, F. Rigoni, R. Mazzaro, M. M. Natile, S. You, V. Morandi, I. Concina, A. Vomiero, *Nano Energy* **2021**, *81*, 105664.

[21] K. Eda, Y. Kato, Y. Ohshiro, T. Sugitani, M. S. Whittingham, *J. Solid State Chem.* **2010**, *183*, 1334.

[22] L. Guo, Z. Yang, K. Marcus, Z. Li, B. Luo, L. Zhou, X. Wang, Y. Du, Y. Yang, *Energy Environ. Sci.* **2018**, *11*, 106.

[23] G. Solomon, R. Mazzaro, S. You, M. M. Natile, V. Morandi, I. Concina, A. Vomiero, *ACS Appl. Mater. Interfaces* **2019**, *11*, 22380.

[24] H. Wan, J. Jiang, X. Ji, L. Miao, L. Zhang, K. Xu, H. Chen, Y. Ruan, *Mater. Lett.* **2013**, *108*, 164.

[25] D. Ghosh, S. Giri, C. K. Das, *Nanoscale* **2013**, *5*, 10428.

[26] V. Fominski, M. Demin, V. Nevolin, D. Fominski, R. Romanov, M. Gritskevich, N. Smirnov, *Nanomaterials* **2020**, *10*, 653.

[27] S. Blomberg, N. Johansson, E. Kokkonen, J. Rissler, L. Kollberg, C. Preger, S. M. Franzén, M. E. Messing, C. Hulteberg, *Materials* **2019**, *12*, 3727.

[28] M. A. Bica De Moraes, B. C. Trasferetti, F. P. Rouxinol, R. Landers, S. F. Durrant, J. Scarmínio, A. Urbano, *Chem. Mater.* **2004**, *16*, 513.

[29] J. Xie, J. Zhang, S. Li, F. Grote, X. Zhang, H. Zhang, R. Wang, Y. Lei, B. Pan, Y. Xie, *J. Am. Chem. Soc.* **2013**, *135*, 17881.

[30] A. E. Reddy, T. Anitha, C. V. V. Muralee Gopi, S. Srinivasa Rao, H. J. Kim, *Dalton Trans.* **2018**, *47*, 9057.

[31] M. Yang, W. Lu, R. Jin, X. C. Liu, S. Song, Y. Xing, *ACS Sustainable Chem. Eng.* **2019**, *7*, 12214.

[32] X. Lin, S. Cao, H. Chen, X. Chen, Z. Wang, S. Zhou, H. Xu, S. Liu, S. Wei, X. Lu, *Chem. Eng. J.* **2021**, *433*, 133524.

[33] X. Yue, W. Ke, M. Xie, X. Shen, Z. Yan, Z. Ji, G. Zhu, K. Xu, H. Zhou, *Catal. Sci. Technol.* **2020**, *10*, 215.

[34] Q. Yang, T. Li, Z. Lu, X. Sun, J. Liu, *Nanoscale* **2014**, *6*, 11789.

[35] T. A. Shifa, K. Yusupov, G. Solomon, A. Gradone, R. Mazzaro, E. Cattaruzza, A. Vomiero, *ACS Catal.* **2021**, *11*, 4520.

[36] X. Huang, X. Cai, D. Xu, W. Chen, S. Wang, W. Zhou, Y. Meng, Y. Fang, X. Yu, *J. Mater. Chem. A* **2018**, *6*, 16890.

[37] Y. Jiang, J. Liu, *Energy Environ. Mater.* **2019**, *2*, 30.

[38] N. Wu, X. Bai, D. Pan, B. Dong, R. Wei, N. Naik, R. R. Patil, Z. Guo, *Adv. Mater. Interfaces* **2021**, *8*, 2001710.

[39] N. R. Chodankar, H. D. Pham, K. Nanjundan, J. F. S. Fernando, K. Jayaramulu, D. Golberg, Y.-K. Han, D. P. Dubal, N. R. Chodankar, Y.-K. Han, H. D. Pham, J. F. S. Fernando, D. Golberg, D. P. Dubal, A. K. Nanjundan, K. Jayaramulu, *Small* **2020**, *16*, 2002806.

[40] M. Huang, X. R. Shi, X. He, X. Zhang, F. Cao, P. Wang, C. Sun, S. Xu, M. Zhang, *Electrochim. Acta* **2022**, *427*, 140884.

[41] S. Huang, X. R. Shi, C. Sun, X. Zhang, M. Huang, R. Liu, H. Wang, S. Xu, *Appl. Surf. Sci.* **2022**, *572*, 151344.